Journal of
Marine Science and Engineering

MDPI

Article

Numerical Study of an Innovative Concept for a Multibody Anti-Pitching Semi-Submersible Floating Wind Turbine

Tianhui Fan, Jianhu Fang, Xinkuan Yan * and Yuan Ma

School of Civil Engineering and Transportation, South China University of Technology, Guangzhou 510641, China; fanth@scut.edu.cn (T.F.); 202120108499@mail.scut.edu.cn (J.F.); scutmy93@163.com (Y.M.)
* Correspondence: ctyanxinkuan@mail.scut.edu.cn

Abstract: The floating offshore wind turbine provides a feasible solution for the development of renewable ocean energy. However, the sizeable rotor diameter of the wind turbine results in large wind heeling moments and pitch amplitude. It will increase the structural loads and cause safety problems. Additionally, the contradictory nature between the stability and the sea-keeping of the floating structure requires that the more flexible method should be adopted to reduce the motion response of the floating offshore wind turbine. Therefore, an innovative concept of a multibody anti-pitching semi-submersible floating offshore wind turbine, named the MBAPSF, is proposed in this paper. The MBAPSF consists of a 5 MW braceless semi-submersible wind turbine and three wave energy converters. The multibody coupled numerical model is established by using an F2A tool, and the dynamic performance of the MBAPSF is compared with that of the traditional semi-submersible wind turbine named the TSSF. The results show that the innovative concept proposed in this paper can reduce pitch motion up to approximately 27% under different load cases, and the maximum bending moment and shearing force at the tower base are also reduced by more than 10%. Meanwhile, WECs are beneficial for increases in the total power generation capacity.

Keywords: floating offshore wind turbine; multibody anti-pitching structure; wave energy converters

Citation: Fan, T.; Fang, J.; Yan, X.; Ma, Y. Numerical Study of an Innovative Concept for a Multibody Anti-Pitching Semi-Submersible Floating Wind Turbine. *J. Mar. Sci. Eng.* **2024**, *12*, 553. https://doi.org/10.3390/jmse12040553

Academic Editor: Spyros A. Mavrakos

Received: 3 February 2024
Revised: 29 February 2024
Accepted: 5 March 2024
Published: 26 March 2024

1. Introduction

Offshore wind power generation plays a major role in the development of renewable energy [1]. Offshore wind power generation has developed significantly in recent years. By the end of 2022, the global offshore wind capacity reached 64.3 GW [2]. With increasing water depth, bottom-fixed offshore wind turbines have become uneconomic and the floating offshore wind turbine (FOWT) has become preferred [3]. The platform types of FOWTs mainly include spar, tension leg platform, barge and semi-submersible. The semi-submersible platform is valued by offshore wind power developers in countries with large continental shelves, such as China, due to their flexibility in operating water depth and structural maturity [4]. However, compared to the traditional floating oil and gas platform, the pitch response of the FOWT is much more significant due to the large aerodynamic load on the rotor. Some results of a tank experiment on the semi-submersible FOWT model have revealed that a maximum pitch inclination of 10° could be reached under the operating conditions [5]. Therefore, it is essential to reduce the pitch motion of the FOWT, which is beneficial to the structural safety.

Meanwhile, the pitch-restoring moment of the floating body is determined by the center of gravity (COG), center of buoyancy (COB) and moment of inertia of the waterplane area. However, for the FOWT, it is difficult to lower the center of gravity and raise the center of buoyancy due to the presence of the towering wind turbine, which results in difficulty in increasing the restoring moment. Therefore, for the pitch and roll motions of the semi-submersible platform, increasing the moment of inertia of the waterplane

area is the recommended method to achieve good dynamic stability [6]. This can be achieved by enlarging the diameter and distance of the columns of the semi-submersible platform. However, it poses a challenge to the structural design of the pontoon and column connections. Additionally, the increase in restoring stiffness also brings the resonant frequency of the platform close to the primary wave frequency region, which is undesirable for the motion performance of the platform. Therefore, it is necessary to propose the design concept of the MBAPSF to balance stability and sea-keeping.

Additionally, the arrangement of the mooring system [7] and the distribution of ballast water between the columns [8] have been taken into account to control the pitch motion of the platform. However, the ballast water approach has a relatively slow dynamic feedback to the environmental loading conditions, and the optimizing mooring system will increase the manufacturing and installation costs.

The controllable connection between the floaters and the platform is an effective approach for improving the stability and the sea-keeping of the FOWT, and this concept is implemented in this paper by combining wave energy converters (WECs) and the FOWT. A similar concept to this is floating wind–wave combined power generation equipment, and earlier equipment has been the STC (Spar–Torus Combination) and SFC (Semi-Submersible Flap Combination) systems proposed by Muliawan [9] and Luan [10]. The STC is a concept combining a spar-type FOWT and a torus (donut-shaped) point absorber-type WEC. The SFC consists of a semi-submersible platform with a 5 MW wind turbine and three flap-type WECs. Relative research results [11–14] have shown that combining point absorber-type WECs with the FOWT seems to have better application prospects. These concepts were originally designed for energy-harvesting performance, with less concern for the effects on platform dynamic stability.

In addition, attaching Wavestar WECs in an array around a semi-submersible platform is another effective way to implement the concept of the floating wind–wave combined power generation equipment [15]. Gaspar et al. [16] and Kamarlouei et al. [17] studied the FOWT, connecting a concentric array of WECs, by using experimental methods. Other researchers [18–20] have followed this idea by combining the Wavestar WEC with the DeepCwind platform, and the main purpose of the above-mentioned concepts is to generate more electricity rather than to be anti-pitching.

From the present research, it was found that the FOWT integrated with the Wavestar WEC could have better motion performances and structural safety compared to the SFC and the STC. The reason is that the flap-type WEC is submerged in water, and the torus point absorber-type WEC is so much closer to the center of gravity of the structure that it is difficult to obtain large moments of inertia. Therefore, the concept of the multibody anti-pitching FOWT proposed in this paper consists of a 5 MW braceless semi-submersible FOWT and three Wavestar WECs. The F2A coupling framework developed by Yang Yang et al. [21] was used to improve the analysis accuracy.

The objective of the present study is to introduce an innovative pitch motion suppression concept, the 'MBAPSF', and compare its pitch motion performance under operating conditions with a traditional semi-submersible FOWT. The results validate the good anti-pitching capability of the MBAPSF. This paper includes five sections. Section 2 presents the design concept of the MBAPSF in detail, and Section 3 introduces the numerical model. The results of the dynamic analysis of the MBAPSF and TSSF are compared and discussed in Section 4. Finally, the conclusions of this study and guidelines for further research are described in Section 5.

2. Design of the Innovation Concept

The MBAPSF consists of a 5 MW braceless semi-submersible FOWT designed by Luan [22] and three Wavestar WECs [23]. The 5 MW wind turbine was developed by the National Renewable Energy Laboratory (NREL). The schematic diagram and main design parameters of the system are shown in Figure 1 and Table 1. Figure 2 shows the top and side views of the MBAPSF (except for the wind turbine and the tower). The braceless

semi-submersible platform is composed of a center column and three side columns. The center column and the side columns are connected by buoyancy tanks. The Wavestar WEC consists of a conical floater and a steel arm, and they are arranged in a polar array around the center column. The steel arm connects the conical floater to the center column. The movement of the floating body drives the steel arm to rotate, which in turn drives the hydraulic power take-off (PTO) to generate electricity. The hydraulic PTO is shown in Figure 3. The PTO system is generally equivalent to the linear damping and stiffness in the numerical simulation [13].

Figure 1. Schematic diagram of the MBAPSF.

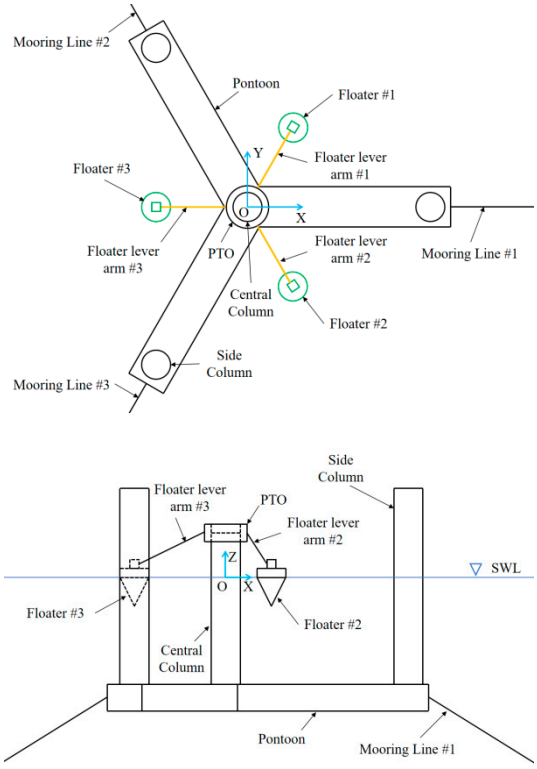

Figure 2. Top (**upper**) and side (**lower**) views of the MBAPSF (except for the wind turbine and the tower).

Table 1. Main design parameters of the MBAPSF.

Item	Property	Value
Wind turbine (NREL 5 MW)	Rotor-nacelle-assembly (t)	350
	Hub height (m)	90
	Tower mass (t)	347.460
Semi-submersible platform	Mass (t)	9738
	Displacement (t)	10,555
	COG (m)	(0, 0, −24.36)
	Diameter of the center column (m)	6.500
	Diameter of the side column (m)	6.500
	Pontoon height (m)	6
	Pontoon width (m)	9
	Operating draft (m)	30
Wavestar WEC	Height/draft (m)	5.25/3.25
	Diameter at the SWL (m)	6.50
	Mass (t)	66.30
	COG (m)	(0, 0, −1.0)
	Displacement (m^3)	70.28
	Length of the steel arm (m)	28
	PTO stiffness (N·m)	3×10^8
	PTO damper (N·m·s)	3×10^9
Mooring system	Number	3
	Angle between adjacent lines (deg)	120
	Diameter (mm)	152
	Length (m)	650
	Weight in air (kg/m)	462.99
	Axial stiffness, EA (kN)	1.973×10^4
	Water depth (m)	100
	Distance from fairleads to SWL (m)	27
	Distance from fairleads to platform centerline (m)	45.95
	Pretension at the fairlead (kN)	1000

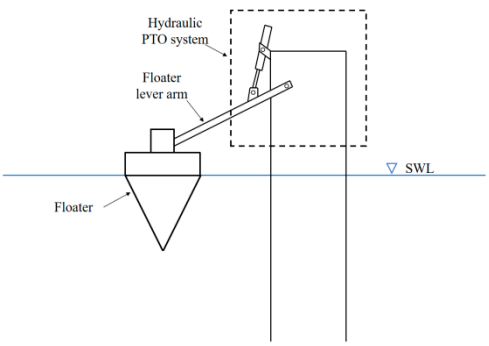

Figure 3. Sketch map of the Wavestar WEC.

3. Numerical Model

The MBAPSF contains several flexible structures, and the coupling effects between these structures complicate the motion response of the FOWT. In addition, the impact of a coupling relationship between multiple environmental loads on the performance of the FOWT must be taken into account. Therefore, it is critical to establish an accurate numerical model for coupled dynamic response analysis of the FOWT involving multiphysics fields and multiple structures.

3.1. Hydrodynamic Model

The 3D potential flow theory was used for frequency-domain hydrodynamic analysis [24]. For the issue of hydrodynamic interaction between multiple floaters, the velocity potential of the fluid can be expressed as [25]:

$$\Phi(\mathrm{x},\mathrm{y},\mathrm{z},\mathrm{t}) = \left[\Phi^{\mathrm{I}}(\mathrm{x},\mathrm{y},\mathrm{z}) + \Phi^{\mathrm{D}}(\mathrm{x},\mathrm{y},\mathrm{z}) + \Phi^{\mathrm{R}}(\mathrm{x},\mathrm{y},\mathrm{z})\right] e^{i\omega t} \tag{1}$$

where $\Phi^{\mathrm{I}}(\mathrm{x},\mathrm{y},\mathrm{z})$ is the incident wave velocity potential; $\Phi^{\mathrm{D}}(\mathrm{x},\mathrm{y},\mathrm{z})$ denotes the diffraction potential and $\Phi^{\mathrm{R}}(\mathrm{x},\mathrm{y},\mathrm{z})$ is the radiation potential. For a structure consisting of multiple floating bodies, the incident potential and diffraction potential generally change slightly in a normal situation, and the radiation potential changes as follows:

$$\Phi^{\mathrm{R}}(\mathrm{x},\mathrm{y},\mathrm{z}) = \sum_{m=1}^{M}\left(\sum_{j=1}^{6} i\omega\xi_j^{(m)}\phi_j^{(m)}\right) \tag{2}$$

where $e^{i\omega t}\xi_j^{(m)}$ represents the displacement of the j^{th} motion modal of the m^{th} floating body; $\xi_j^{(m)}$ is the corresponding motion amplitude and $\phi_j^{(m)}$ represents the unit velocity potential induced by the j^{th} modal motion of the m^{th} floating body. The boundary value conditions should be satisfied as follows:

$$\begin{cases} \dfrac{\partial^2\phi_j^{(m)}}{\partial x^2} + \dfrac{\partial^2\phi_j^{(m)}}{\partial y^2} + \dfrac{\partial^2\phi_j^{(m)}}{\partial z^2} = 0 \\ g\dfrac{\partial\phi_j^{(m)}}{\partial \mathrm{z}} - \omega^2\phi_j^{(m)} = 0 \quad \text{Free surface} \\ \dfrac{\partial\phi_j^{(l)}}{\partial n} = \begin{cases} n_j^{(m)} & l = m \\ 0 & l \neq m \end{cases} \quad \text{Body surface} \\ \left.\dfrac{\partial\phi_j^{(m)}}{\partial \mathrm{z}}\right|_{\mathrm{z}=-\mathrm{H}} = 0 \quad \text{Seabed surface} \\ \lim\limits_{r\to\infty}\sqrt{r}\left[\dfrac{\partial\phi_j^{(m)}}{\partial \mathrm{r}} - ik\phi_j^{(m)}\right] = 0 \quad \text{Infinite distance} \end{cases} \tag{3}$$

where x, y, z are the displacements in three directions of the coordinate axis, respectively; t is time; $\frac{\partial}{\partial n}$ is the partial derivative with respect to the normal direction along the surface of the floating body; H is the sea depth; and $r = \sqrt{x^2 + y^2}$; k is the wave number, which satisfies the dispersion relation $\omega^2 = gk\tanh kH$.

After obtaining the diffraction potential and radiation potential, the first-order hydrodynamic pressure distribution of the floating body can be obtained from Bernoulli's equation. Then, the first-order wave excitation force on the floating body can be calculated by integrating the pressure over the surface of the floating body. The movements of the FOWT are significantly affected by the second-order wave force. The mean wave drift force was calculated by the far-field method in this study. The reason is that the operating water depth of the FOWT was moderate and the far-field method is more computationally efficient compared to the near-field method [24].

The potential flow theory assumes that fluid is inviscid; it cannot analyze the impact of fluid viscosity on an offshore floating structure. In this study, the Morison model was used to calculate the viscous load applied to the cylinder of the semi-submersible platform, which can be expressed as follows [26]:

$$f_d = C_d \frac{\rho_w}{2} D v|v| \tag{4}$$

where f_d is the drag force; C_d is the drag force coefficient, where $C_d = 1.2$ [27] is selected in this paper; and D and v are the structure diameter and flow velocity, respectively.

The calculation formula for the viscous load applied to the WEC is as follows [28,29]:

$$D_{critical} = 2\sqrt{(M + \Delta M)K} \tag{5}$$

$$F_{viscous} = D_{critical} \times \mu \tag{6}$$

where M and ΔM represent the generalized mass in the vertical plane and the additional generalized mass in the vertical plane at the resonant frequency, respectively; K is the hydrostatic stiffness in the vertical plane; and μ denotes the damping coefficient. Generally, the damping coefficient can be taken as 5–10%, and the value is defined as 8% in this study [30].

3.2. Aerodynamic Model

The blade element method (BEM) is used to calculate wind thrust and torque on the wind turbine rotor. The BEM assumes that there is no interaction between different blade elements and the stress on the blade section represents the stress on the entire blade element. The rotor thrust, T, and torque, Q, can be expressed as [18]:

$$\mathrm{d}T = \frac{1}{2}\rho_a W^2 N(C_L cos\varphi + C_d sin\varphi)\mathrm{d}r \tag{7}$$

$$\mathrm{d}Q = \frac{1}{2}\rho_a W^2 N(C_L cos\varphi + C_d sin\varphi) r\mathrm{d}r \tag{8}$$

where W is the relative inflow wind speed; N is the number of blade elements; and C_L and C_d donate the lift and drag coefficients of the blade element airfoil, respectively. φ is the inflow angle, and r is the radius of the blade. The aerodynamic coefficients under unsteady conditions are corrected based on the Beddoes–Leishman dynamic stall model. Finally, by integrating the forces on the blade elements, the total thrust and torque of the overall rotor can be obtained. More details about this theory can be found in the AeroDyn Theory Manual published by NREL [31].

3.3. Mooring System Model

The lumped-mass method is applied for the dynamic analysis of mooring lines. The method is to discretize the mooring line into a series of segments regarded as massless springs joined together by mass nodes and then perform a finite difference solution to the equilibrium control differential equation. The dynamics equation of the mooring lines can be expressed as [32]:

$$m_i \ddot{r}_i = F_{b_i} + W_i + T_i + C_i + F_{M_i} + F_{S_i} \tag{9}$$

where m_i is the mass of the i^{th} node; $\ddot{r}_i$,F_{b_i} and W_i are the acceleration, buoyancy and gravity of the i^{th} node, respectively; and T_i, C_i, F_{M_i} and F_{S_i} are the axial tension, damping force, additional mass force and seabed friction force, respectively. A more detailed explanation of the lumped-mass method can be found in the AQWA Theory Manual [24].

3.4. Equation of Motion

In this study, the MBAPSF consists of four bodies and each body has 6 degrees of freedom. Therefore, a comprehensive consideration of the multiple degree of freedom (DOF) system is necessary [33]. The multibody motion equation is shown as follows [12]:

$$\begin{aligned}
&\begin{bmatrix} M^{(1)}+\mu^{(11)} & \cdots & \mu^{(41)} \\ \vdots & \ddots & \vdots \\ \mu^{(14)} & \cdots & M^{(4)}+\mu^{(44)} \end{bmatrix} \begin{Bmatrix} \ddot{x}^{(1)}(t) \\ \vdots \\ \ddot{x}^{(4)}(t) \end{Bmatrix} \\
&+\int_0^t \begin{bmatrix} k(t-\tau)^{(11)} & \cdots & k(t-\tau)^{(14)} \\ \vdots & \ddots & \vdots \\ k(t-\tau)^{(41)} & \cdots & k(t-\tau)^{(44)} \end{bmatrix} \begin{Bmatrix} \dot{x}^{(1)}(\tau) \\ \vdots \\ \dot{x}^{(4)}(\tau) \end{Bmatrix} d\tau \\
&+\begin{bmatrix} C^{(1)} & \cdots & 0 \\ \vdots & \ddots & \vdots \\ 0 & \cdots & C^{(4)} \end{bmatrix} \begin{Bmatrix} x^{(1)}(t) \\ \vdots \\ x^{(4)}(t) \end{Bmatrix} \\
&=\begin{bmatrix} f_{wind}(t) \\ \vdots \\ 0 \end{bmatrix} + \begin{bmatrix} f_{wave}^{(1)}(t) \\ \vdots \\ f_{wave}^{(4)}(t) \end{bmatrix} + \begin{bmatrix} f_{vis}^{(1)}(t) \\ \vdots \\ f_{vis}^{(4)}(t) \end{bmatrix} + \begin{bmatrix} f_{PTO}^{(1)}(t) \\ \vdots \\ f_{PTO}^{(4)}(t) \end{bmatrix} \\
&+\begin{bmatrix} f_{mooring}(t) \\ \vdots \\ 0 \end{bmatrix}
\end{aligned} \tag{10}$$

where the superscripts (1) and (11) refer to the variables of body 1 (the platform) and the superscripts (2)–(4) and (22)–(44) refer to the variables of bodies 2–4 (the WECs). M and μ are the generalized mass and the generalized added mass at the infinite wave frequency, respectively. $\ddot{x}$, $\dot{x}$ and x are the acceleration, velocity and displacement in the time domain, respectively. k is the radiation impulse response function. t and τ are time terms. C denotes the hydrostatic restoration coefficient.

3.5. Coupled Model

The fully coupled time-domain numerical model was constructed in this study based on the F2A simulation tool, which was proposed by Yang et al. [21]. As can be seen from Figure 4, the tower base load calculated by the FAST (version 7.03) subroutines is transmitted to AQWA (version 2023 R1) in the form of external force through DLL. Similarly, the platform motion response calculated by AQWA will also be transmitted back to the FAST subroutine program to determine the wind turbine aerodynamic load. More details about the fully coupled analysis tool F2A can be found in the paper published by Yang Yang et al. in 2020 [21]. The analysis framework of the F2A simulation tool is shown in Figure 4. This simulation tool has been used and verified by many scholars [7,18,21,25,34].

Different connection forms are used between the FOWT and WEC in order to better calculate the coupled dynamic responses. The PTO system of the WEC can be regarded as a spring-damper system. In AQWA, the connect joint is used to connect the WEC float and platform and the stiffness and damping coefficients of the joint are defined as K_{PTO} and B_{PTO}, respectively.

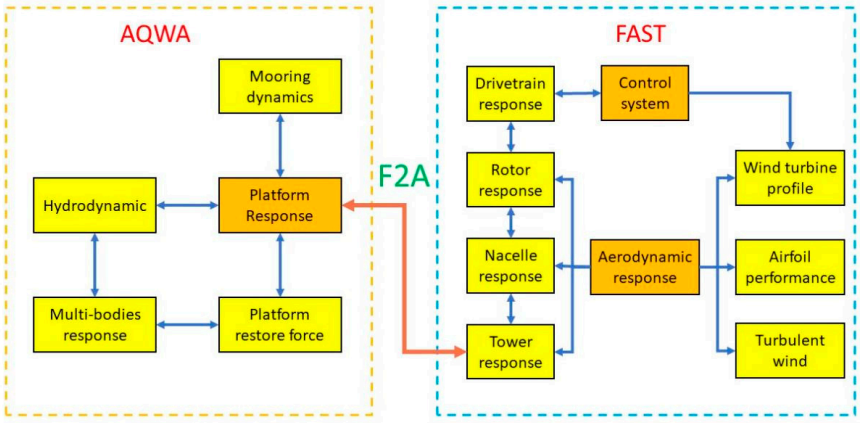

Figure 4. Flowchart of the fully coupled analysis method.

3.6. Numerical Model Validation

To verify the accuracy of the F2A simulation tool, validation was conducted by comparing the numerical simulation results and the model test results of the benchmark OC4 DeepCwind [35,36].

The typical environmental conditions are shown in Table 2. The statistical results obtained by the F2A simulation tool and model test are summarized in Table 3. The mean values of the motion responses in the surge, heave and pitch of the numerical model have relative errors of −5.61%, −6.53% and −5.95% compared with those of the model test results, respectively. Further investigation of the statistical results showed that the numerical results slightly underestimated the platform motion response compared with the model test results. In general, the results obtained through the model test and the numerical results are in good agreement, indicating the reliability of the F2A tool and the accuracy of the fully coupled numerical model used in this paper.

Table 2. Environmental conditions of test conditions.

Items	Values
Wave Spectrum	Jonswap
Significant Wave Height	7.1 m
Spectral Peak Period	12.1 s
Peak Factor	2.2
Steady Wind Speed	16.11 m/s

Table 3. Statistical results of the OC4 DeepCwind platform motion response.

Items		Model Test Results	Numerical Results	Errors
Surge (m)	Max	14.100	13.078	−7.25%
	Min	1.530	1.582	3.42%
	Mean	5.900	5.569	−5.61%
Heave (m)	Max	2.170	2.056	−5.24%
	Min	−2.160	−2.019	−6.53%
	Mean	0.071	0.0708	−0.28%
Pitch (°)	Max	4.900	4.473	−8.71%
	Min	−1.170	−0.990	−15.42%
	Mean	1.870	1.759	−5.95%

4. Results and Discussion

4.1. Free Decay Test

The time histories of the free decay tests in surge are shown in Figure 5, and the natural periods of six DOFs are listed in Table 4. It can be seen that the additional

multibody structure significantly reduced the natural periods of the platform in the heave and pitch DOFs, which illustrates that the restoring forces/moments in the two DOFs were increased.

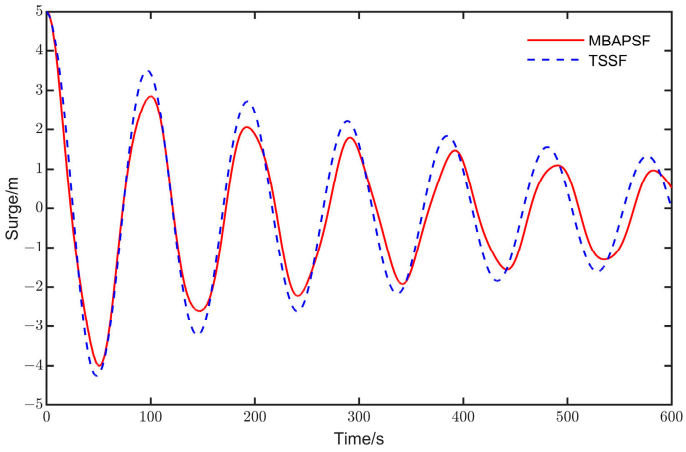

Figure 5. Time history of surge decay test.

Table 4. Natural periods of the TSSF and the MBAPSF.

DOF	TSSF	MBAPSF
Surge/Sway	96.66 s	98.86 s
Heave	26.00 s	20.40 s
Roll/Pitch	35.95 s	30.31 s
Yaw	73.48 s	70.89 s

4.2. Time-Domain Fully Coupled Analysis

4.2.1. Environmental Condition

Table 5 shows the environmental conditions used in this study. In order to better investigate the anti-pitching ability of the MBAPSF, the wind velocity was set to 11.4 m/s, which enabled the wind turbine to generate the maximum thrust. According to the ABS, the IEC turbulent wind model NTM is recommended to analyze the dynamic responses of the FOWT under operating conditions [37]. The turbulence intensity was set to 0.14, and the wind speed represents the 10 min mean wind speed at the wind turbine hub. From DNVGL-RP-C205 [38], the JONSWAP spectrum was used to generate the irregular wave time series, and its spectral peak factor was taken as 3.3. Both the incident directions of the wind and wave were 0°.

Table 5. Environmental conditions.

Load Case	Wind Velocity, V_{wind}	Wave Height, H_s	Wave Period, T_p
LC1	11.4 m/s	1.7 m	5.7 s
LC2	11.4 m/s	3.0 m	10.0 s
LC3	11.4 m/s	4.2 m	10.2 s

4.2.2. Platform Motion Responses

In this section, the floating platform motion responses of the MBAPSF and TSSF under different load cases (LCs) are compared and analyzed. The surge, heave and pitch are the most important DOFs for the FOWT. The total simulation duration was 6000 s. In order to avoid transient effects, the first 800 s were ignored.

The responses of motion and mooring line tension under the operation conditions of LC2 are shown in Figures 6 and 7. The drift force time histories and PSDs of the MBAPSF and the TSSF under LC2 can be seen in Figure 8. The statistical results of the

platform motions and the mooring line tension in different load cases are presented in Table 6. The surge response of the MBAPSF is slightly larger than that of the TSSF, as shown in Figure 6a and Table 6. Additionally, the increase in the mooring tension of the MBAPSF was within 9% compared to the TSSF. As shown in the PSD of the platform surge and mooring lines, the WECs resulted in the increase in low-frequency responses on the MBAPSF. This is also verified in Figure 8. The drift force of the MBAPSF is larger at low frequencies compared to the TSSF. As Figure 6c and Table 6 represent, compared to the TSSF, there was a significant reduction in the pitch response for the MBAPSF. Both the maximum and mean values of the pitch motion were reduced by approximately 27% under the different environmental conditions in this paper, which means that WECs can amplify the restoring moment. As revealed in Figure 7c, the resonant response peak of the pitch motion of the MBAPSF is significantly smaller than that of the TSSF. In addition, Figure 6b and Table 6 show that WECs can restrain the heave motion of the platform, and there is an obvious reduction in wave frequency response, as shown in Figure 7b. This indicates that compared to the TSSF, there is greater restoring stiffness and damping in the heave direction for the MBAPSF.

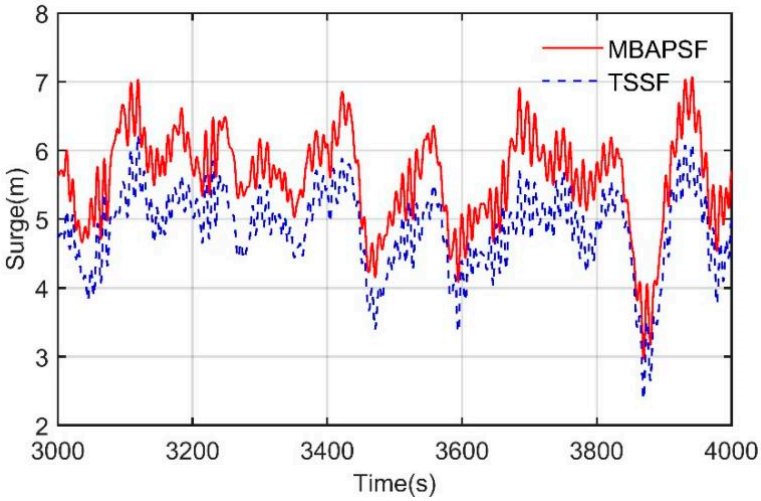

(**a**) Surge.

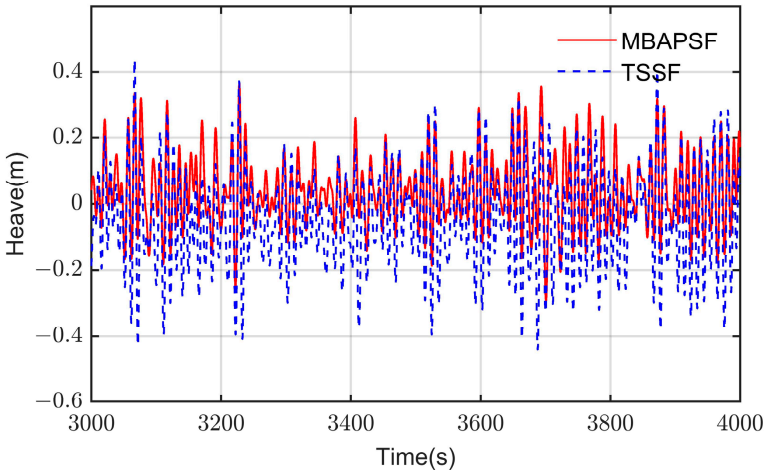

(**b**) Heave.

Figure 6. *Cont.*

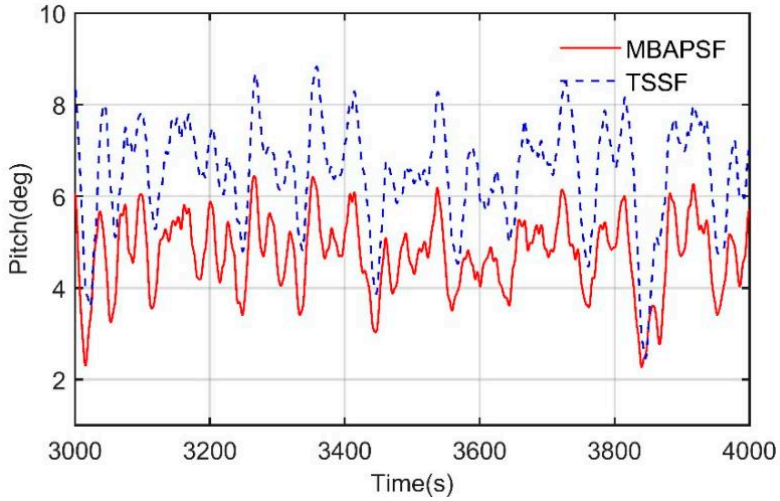

(**c**) Pitch.

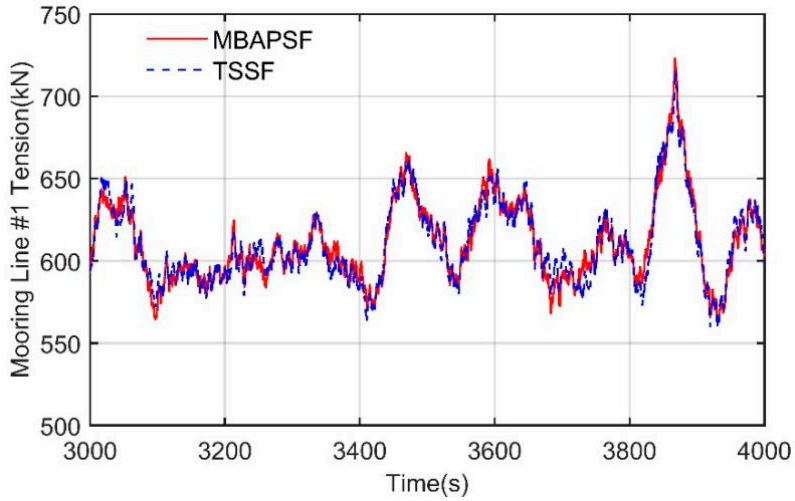

(**d**) Mooring Line #1 tension.

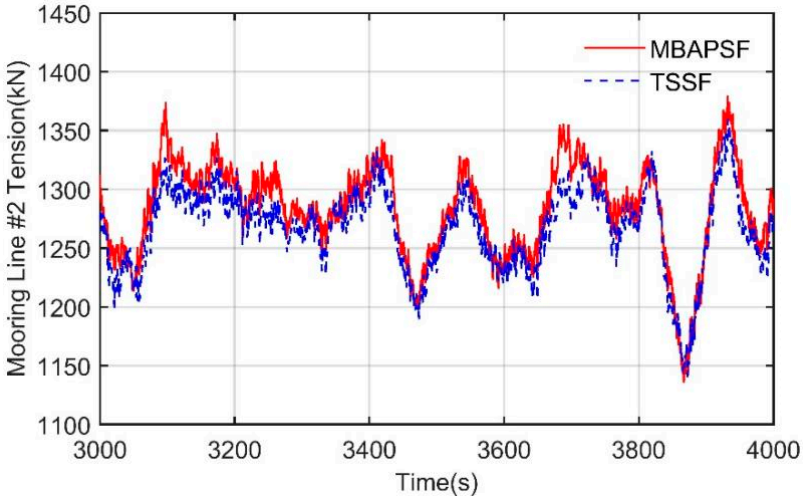

(**e**) Mooring Line #2 tension.

Figure 6. *Cont.*

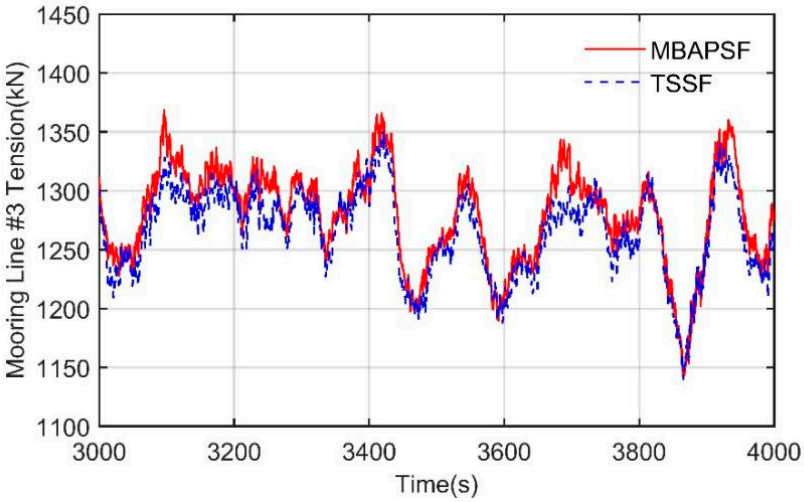

(**f**) Mooring Line #3 tension.

Figure 6. The time history of the platform motion and mooring line tension of the MBAPSF and TSSF under LC2.

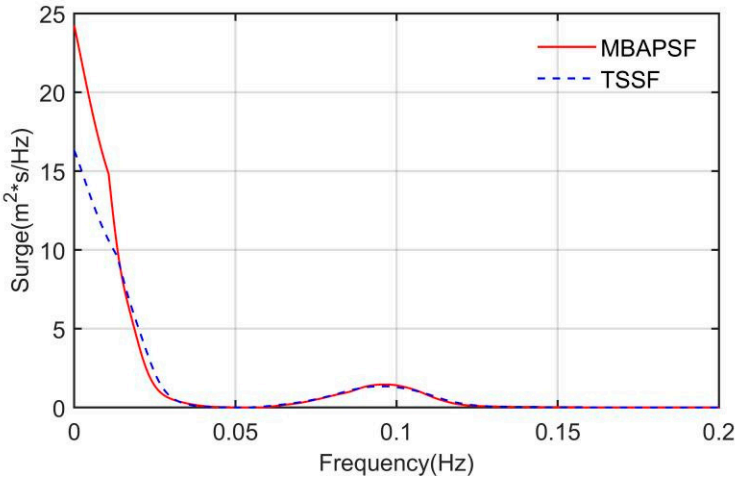

(**a**) Surge.

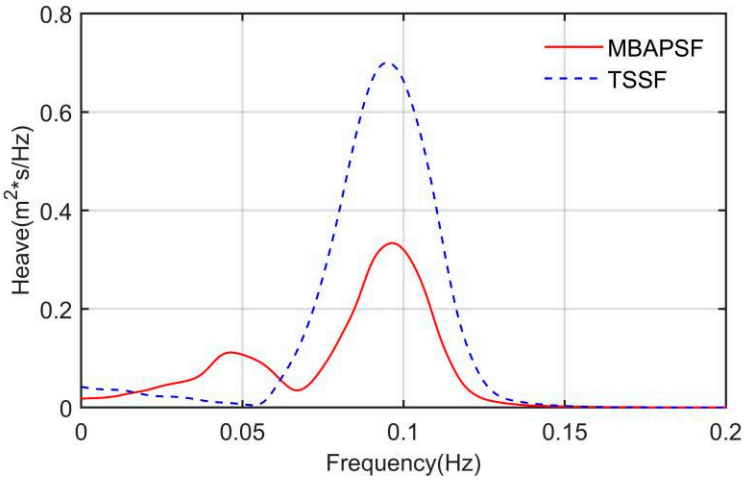

(**b**) Heave.

Figure 7. *Cont.*

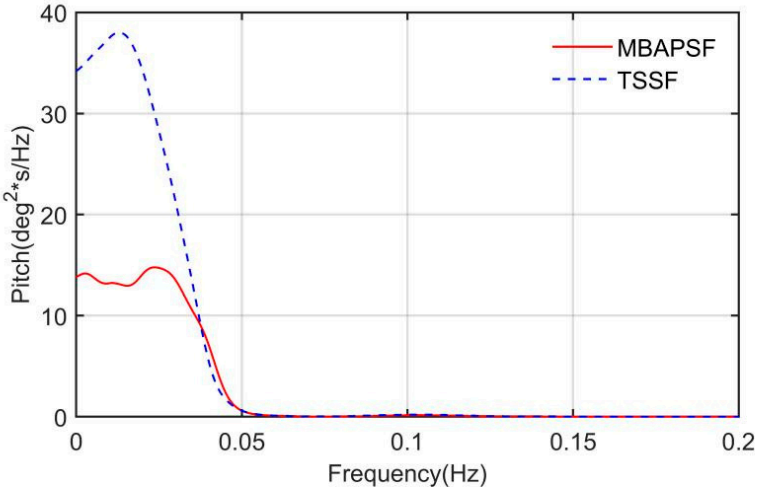

(**c**) Pitch.

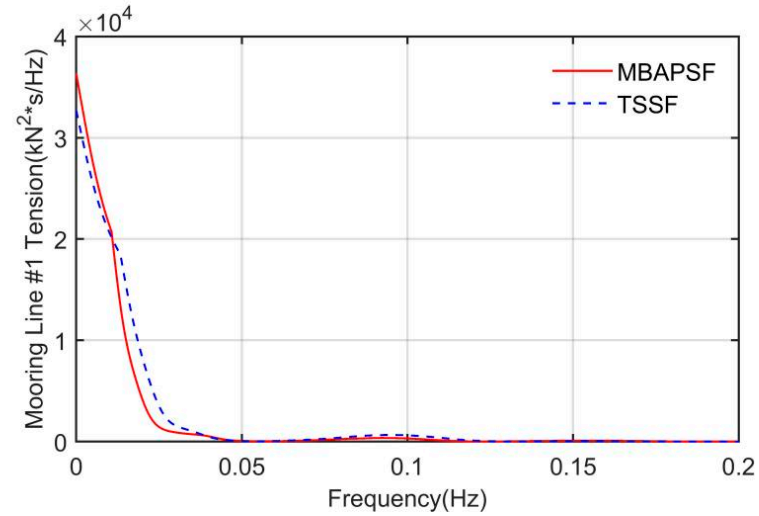

(**d**) Mooring Line #1 Tension.

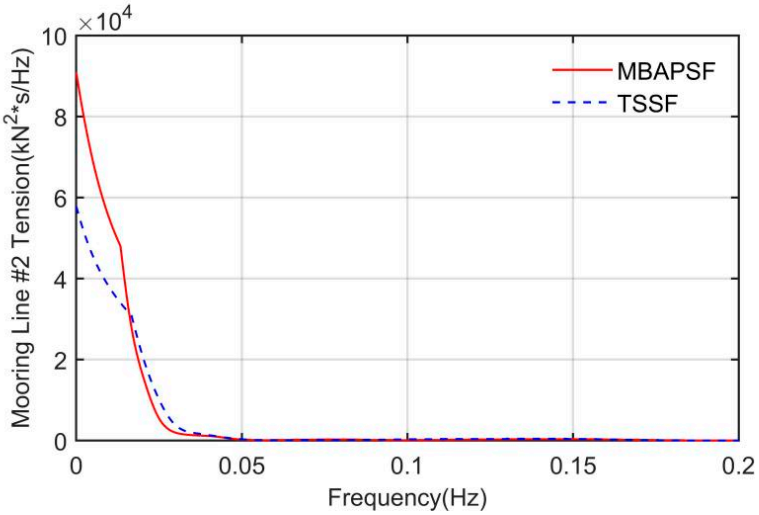

(**e**) Mooring Line #2 Tension.

Figure 7. *Cont.*

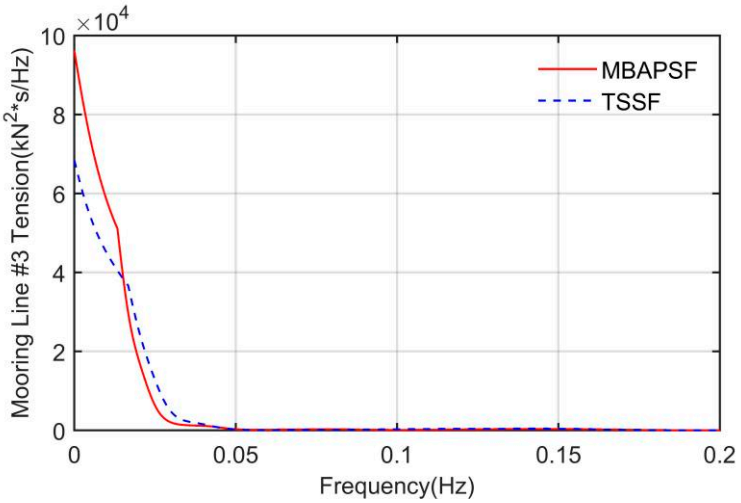

(**f**) Mooring Line #3 Tension.

Figure 7. The response PSDs of the platform motion and mooring tension of the MBAPSF and TSSF under LC2.

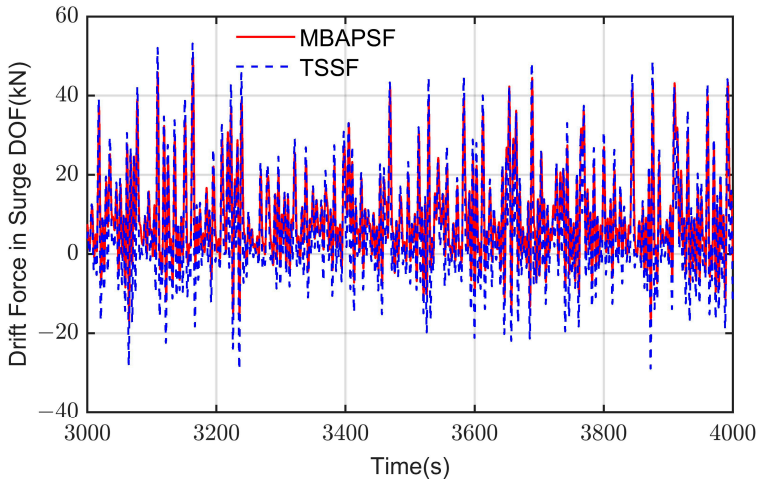

(**a**) Surge.

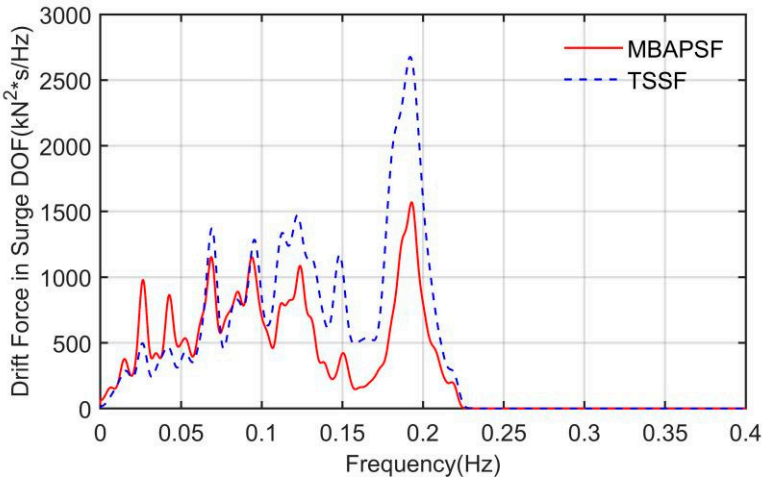

(**b**) Surge PSD.

Figure 8. The drift force time history and PSDs of the MBAPSF and TSSF under LC2.

Table 6. Statistical results of the platform motions and the mooring line tension under different load cases.

Items		LC1		LC2		LC3	
		TSSF	MBAPSF	TSSF	MBAPSF	TSSF	MBAPSF
Surge (m)	Max	6.04	6.99	6.54	7.47	7.73	9.91
	Mean	4.91	5.61	4.91	5.67	5.29	6.38
	STD	0.63	0.68	0.56	0.63	0.68	0.87
Heave (m)	Max	0.08	0.14	0.51	0.62	0.77	0.94
	Mean	−0.05	0.02	−0.05	0.04	−0.05	0.05
	STD	0.04	0.03	0.16	0.12	0.25	0.19
Pitch (deg)	Max	9.92	7.24	9.72	7.08	9.63	7.03
	Mean	6.62	4.79	6.61	4.79	6.63	4.84
	STD	1.14	0.84	1.07	0.78	1.04	0.78
Mooring Line #1 Tension (kN)	Max	703.93	697.72	715.36	723.11	692.23	684.33
	Mean	607.95	609.58	607.34	607.86	595.03	586.62
	STD	26.24	25.08	23.47	23.13	24.31	26.24
Mooring Line #2 Tension (kN)	Max	1379.82	1384.9	1359.55	1406.11	1417.93	1545.45
	Mean	1270.93	1282.82	1271.78	1287.45	1293.48	1331.97
	STD	38.13	40.26	23.37	37.48	37.58	51.94
Mooring Line #3 Tension (kN)	Max	1373.72	1379.71	1365.91	1412.96	1425.43	1551.72
	Mean	1269.47	1280.46	1270.04	1284.28	1291.54	1328.15
	STD	41.08	42.93	35.55	39.06	39.83	39.06

4.2.3. Wind Turbine Dynamic Responses

The shear force and bending moment at the tower base are the most crucial structural loads, as they easily lead to problems in structural integrity and longevity. The influences of WECs on the tower base shear force and the bending moment of the FOWT were investigated, and the results are shown in Figures 9 and 10 and Table 7. Different environmental conditions were involved in this investigation, and only the dynamic responses under LC2 are presented in the figures below. It can be seen that the loads at the tower base decreased obviously under the effects of the WECs. The statistical values of the shear force and bending moment were all reduced by about 10% under different environmental loads, which is beneficial for improving the safety of the tower structure. Figure 10 reveals that the WEC had great effects on the low-frequency structural loads. The comparison shown in Table 7 demonstrates that the wind power generation capacity of the two systems is almost the same.

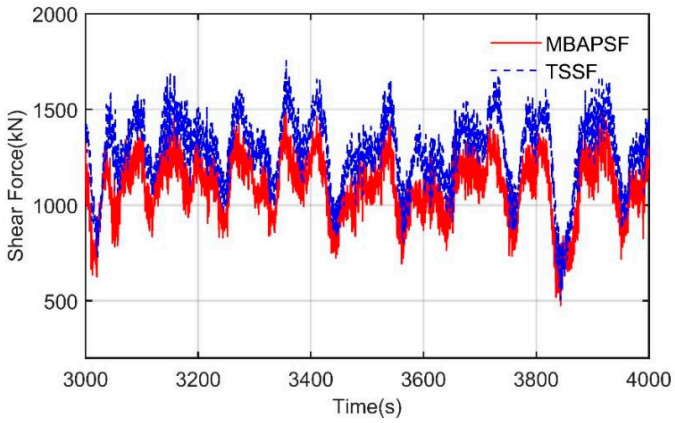

(**a**) Shear force.

Figure 9. *Cont.*

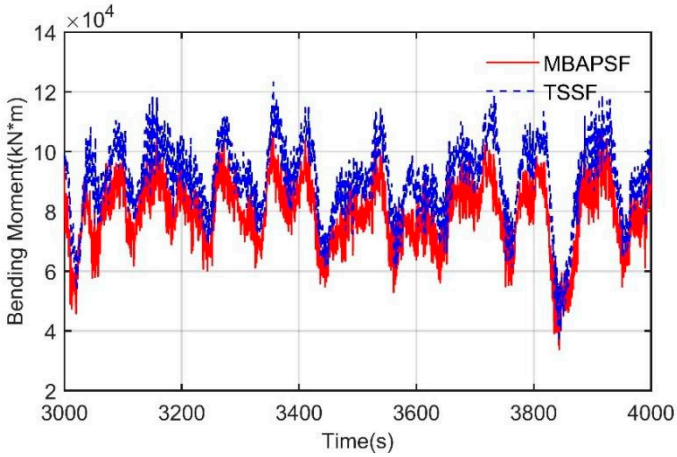

(**b**) Bending moment.

Figure 9. The tower base loads of the MBAPSF and TSSF under LC2.

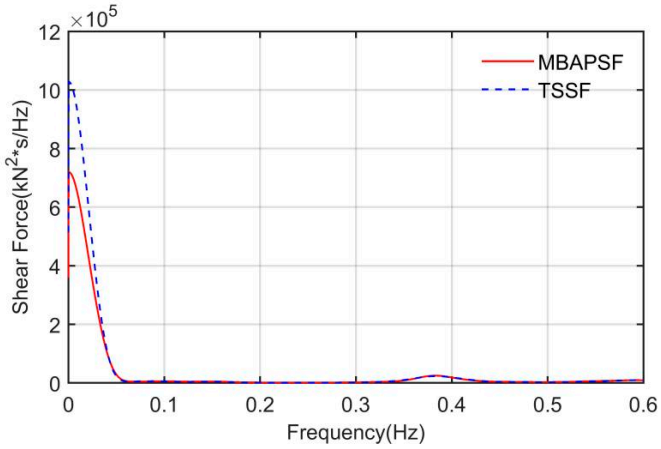

(**a**) Shear force.

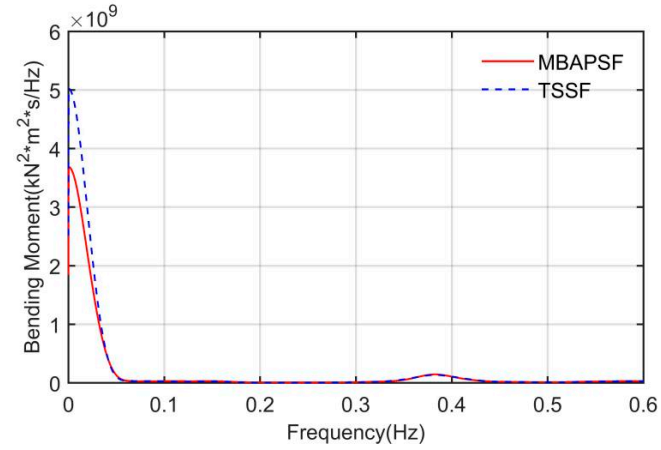

(**b**) Bending moment.

Figure 10. The PSDs of the tower base loads of the MBAPSF and TSSF under LC2.

Table 7. Statistical results of wind turbine dynamic responses under different c·onditions.

Items		LC1			LC2			LC3		
		TSSF	MBAPSF	Difference	TSSF	MBAPSF	Difference	TSSF	MBAPSF	Difference
Wind power capacity (kW)	Mean	4570.75	4600.94	0.66%	4572.05	4601.25	0.64%	4570.90	4601.21	0.66%
	STD	621.22	608.07	−2.12%	621.66	611.91	−1.57%	623.03	614.89	−1.31 %

Table 7. *Cont.*

Items		LC1			LC2			LC3		
		TSSF	MBAPSF	Difference	TSSF	MBAPSF	Difference	TSSF	MBAPSF	Difference
Tower base shear force (kN)	Max	1788.00	1573.00	−12.02%	1771.00	1537.00	−13.26%	1747.00	1557.00	−10.88%
	Min	499.80	487.10	−2.54%	505.40	476.1	−5.80%	589.00	521.80	−11.41%
	Mean	1295.03	1109.96	−14.29%	1294.57	1108.96	−14.34%	1296.71	1113.62	−14.12%
	STD	181.85	155.18	−14.66%	177.00	151.89	−14.19%	177.00	152.12	−14.06%
Tower base bending moment (MN·m)	Max	125.70	112.50	−10.50%	124.80	110.10	−11.78%	121.90	110.20	−9.60%
	Min	35.61	35.83	0.62%	36.13	33.84	−6.34%	41.03	38.74	−5.58%
	Mean	91.52	80.16	−12.41%	91.49	80.10	−12.46%	91.62	80.38	−12.27%
	STD	12.48	10.87	−12.92%	12.19	11.36	−6.81%	12.04	10.69	−11.19%

4.2.4. WEC Response

For the PTO system of the Wavestar WEC, the PTO force and the wave energy power produced by the PTO can be expressed as [18,23]:

$$f_{pto} = B_{pto} \cdot \omega_{arm} + K_{pto} \cdot \theta_{arm} \tag{11}$$

$$P_{pto} = f_{pto} \cdot \omega_{arm} \tag{12}$$

where ω_{arm} and θ_{arm} represent the rotation velocity and rotation angle of the steel arm of the Wavestar, respectively.

Figure 11 shows the force/moment of the PTOs applied to the heave and pitch DOFs of the platform under LC2. Table 8 shows the total power generation capacity (the sum of the wind and wave power generation capacities) of the TSSF and the MBAPSF under different environmental conditions. From Figure 11a,b, we can find that WECs arranged at different locations had different effects on the heave and pitch DOFs of the platform. For the heave DOF, the WECs arranged at the downwind side (i.e., WEC #2 and #3) provided more additional restoring force, and the WEC in the other direction (i.e., WEC #1) played the opposite role. The reason is that the large wind heeling moment generated by the wind turbine makes the pitch angle of the platform always face the downwind direction, which causes the WECs arranged in this direction to always be in a submerged condition; that is, the rotation angle of the Wavestar steel arm during movement is generally smaller than the initial angle. The opposite is true for WECs arranged in the upwind direction. For the pitch DOF, the results revealed that the WECs arranged at different positions all had an effect on decreasing the motion response of the platform, and the effect from the WECs at the upwind side was greater. The differences of the total power generation capacity between the TSSF and the MBAPSF are highlighted in Figure 10c. Compared to the TSSF, the total power generation capacity of the MBAPSF under different LC1, LC2 and LC3 conditions increased by 8.82%, 9.27% and 10.44%, respectively. It is obvious that as the wave load increases, the increase rate of the total power generation capacity of the system increases.

Table 8. Statistical results of WEC responses under different conditions.

Items		LC1	LC2	LC3
Sum of the WEC forces applied on the platform in heave DOF (kN)	Max	680.94	1721.88	2574.46
	Min	−452.50	−1114.79	−1614.15
	Mean	87.92	108.04	144.11
	STD	151.97	399.43	576.34
Sum of the WEC moments applied on the platform in pitch DOF (kN·m)	Max	1182.74	4371.06	7523.70
	Min	−26,018.55	−30,332.20	−37,067.49
	Mean	−14,103.37	−14,144.17	−14,287.98
	STD	3764.23	4676.51	5894.96
Wave power	Mean	394.53	446.97	559.20

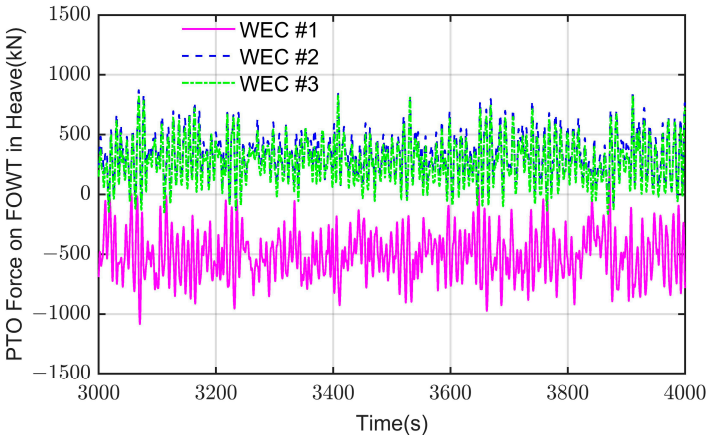

(**a**) PTO force on FOWT in heave.

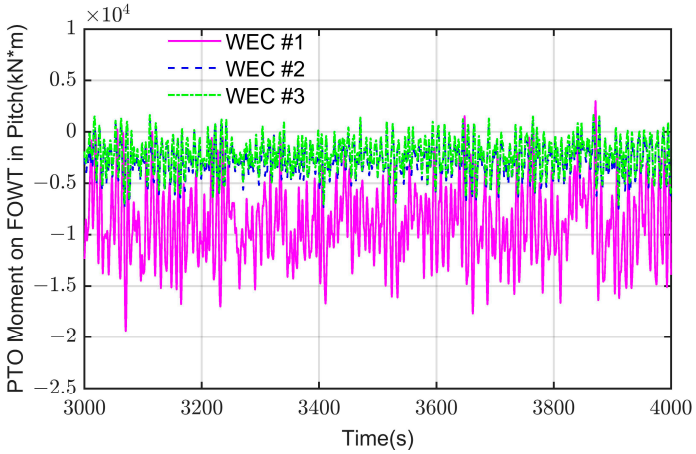

(**b**) PTO Moment on FOWT in pitch.

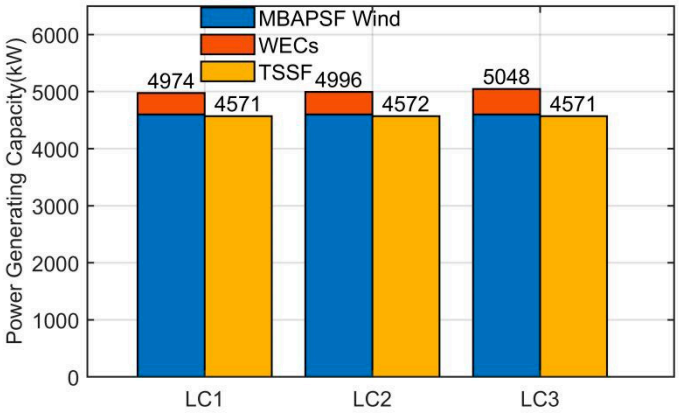

(**c**) Power generating capacity.

Figure 11. Load responses of the WECs and the power generating capacity under LC2.

5. Conclusions

The innovative concept of the multibody anti-pitching semi-submersible wind turbine, the 'MBAPSF', is proposed in this study. The MBAPSF is composed of a 5 MW braceless semi-submersible FOWT and three Wavestar WECs. The fully coupled numerical model of the MBAPSF was established by using the F2A simulation tool. Furthermore, investigation of the dynamic performances of the MBAPSF under various environmental conditions was conducted, and the results are compared to the traditional 5 MW semi-submersible FOWT,

referred to as the TSSF. The superior and inferior aspects of the innovative concept have been discussed, and the main conclusions are drawn as follows:

(1) The Wavestar WECs can suppress the motion response of the platform and significantly improve the pitch stability. The maximal and mean pitch motion were reduced by approximately 27%. However, the addition of the waterline area of the platform led to an increase in the low-frequency drifting force in waves, which slightly raised the surge motion amplitude and mooring line tension.
(2) Compared to the TSSF, the dynamic responses of the shear force and bending moment at the tower base of the MBAPSF under different conditions decreased significantly, which is beneficial for the structural life.
(3) The different position layouts of the WECs had different effects on the additional restoring force/moment in the heave and pitch DOFs of the platform. The heave response of the platform was mainly reduced by the WECs at the downwind side. The WECs arranged at different positions all contributed to the anti-pitching, and the effect from the WEC at the upwind side was greater.
(4) Compared to the TSSF, the total power generation capacities of the MBAPSF under different environmental conditions increased by 8.82%, 9.27% and 10.44%, respectively. Wind energy generation capacity still accounts for a major part of the total power generation capacity of the MBAPSF system. Thus, the main target of adding WECs is to reduce the system motion response and increase structural safety.

The MBAPSF concept proposed in this paper is fundamentally planned to reduce the pitch motion of the FOWT and improve the structure's safety. However, there are some limitations in this study that should be further researched in the future. For example, the optimal design of the damping coefficient of the PTO system should be explored to improve the motion performance. Additionally, the influences of different control strategies of the wind turbine on the anti-pitching effect for the MBAPSF can be carried out in future work. Moreover, the PTO system of WECs arranged at different positions can be given different damping and stiffness coefficients to improve the platform motion performances in future research.

Author Contributions: Conceptualization, T.F., J.F., X.Y. and Y.M.; methodology, T.F., J.F., X.Y. and Y.M.; software, T.F. and J.F.; validation, T.F. and J.F.; formal analysis, T.F. and J.F.; investigation, T.F., J.F., X.Y. and Y.M.; writing—original draft preparation, T.F., J.F. and X.Y.; writing—review and editing, T.F., J.F., X.Y. and Y.M.; visualization, J.F. and X.Y.; supervision, T.F.; project administration, T.F. and X.Y.; funding acquisition, T.F. All authors have read and agreed to the published version of the manuscript.

Funding: This study was financially supported by the Natural Science Foundation of Guangdong Province, China (Grant No. 2022B1515020071); the National Natural Science Foundation of China (Grant No. 52071145, 52001126); the Fundamental Research Funds for the Central Universities (Grant No. 2023ZYGXZR029); and the Guangdong province science and technology project (Grant No. 2021A0505030006).

Data Availability Statement: Date are available upon request.

Conflicts of Interest: The authors declare no conflicts of interest.

Abbreviations

The following abbreviations are used in this manuscript:

FOWT	Floating offshore wind turbine
MBAPSF	Multibody anti-pitching semi-submersible wind turbine
TSSF	Traditional semi-submersible FOWT
WEC	Wave energy converter
STC	Spar–Torus Combination
SFC	Semi-Submersible Flap Combination
SWL	Still water level
BEM	Blade element method

PTO	Power take-off
STD	Standard deviation
ABS	American Bureau of Shipping
IEC	International Electrotechnical Commission
NTM	Normal turbulence model
DOF	Degree of freedom
PSD	Power spectral density
LC	Load case
ω	Rotational frequency of wave
g	Acceleration of gravity
ρ_w	Water density
ρ_a	Air density
$F_{viscous}$	Viscous force
$D_{critical}$	Critical damping
f_{wind}	Wind drag force
f_{wave}	Wave force
f_{vis}	Fluid viscous force
f_{PTO}	PTO force
$f_{mooring}$	Mooring force
P_{pto}	Wave energy power produced by the PTO
B_{pto}	PTO damping coefficient
K_{pto}	PTO stiffness coefficient

References

1. Chen, C.; Ma, Y.; Fan, T. Review of model experimental methods focusing on aerodynamic simulation of floating offshore wind turbines. *Renew. Sustain. Energy Rev.* **2022**, *157*, 112036. [CrossRef]
2. Williams, R.; Bath, A. *Global Offshore Wind Report 2023*; Global Wind Energy Council: Lisbon, Portugal, 2023.
3. Subbulakshmi, A.; Verma, M.; Keerthana, M.; Sasmal, S.; Harikrishna, P.; Kapuria, S. Recent advances in experimental and numerical methods for dynamic analysis of floating offshore wind turbines—An integrated review. *Renew. Sustain. Energy Rev.* **2022**, *164*, 112525. [CrossRef]
4. Liu, Y.; Li, S.; Yi, Q.; Chen, D. Developments in semi-submersible floating foundations supporting wind turbines: A comprehensive review. *Renew. Sustain. Energy Rev.* **2016**, *60*, 433–449. [CrossRef]
5. Zhu, H.; Hu, C. A study on control of wave energy converter for motion suppression of semisubmersible. *IFAC-Pap.* **2016**, *49*, 380–385. [CrossRef]
6. Cheng, Z.; Wang, K.; Gao, Z.; Moan, T. Dynamic response analysis of three floating wind turbine concepts with a two-bladed Darrieus rotor. *J. Ocean. Wind. Energy* **2015**, *2*, 213–222. [CrossRef]
7. Ma, Y.; Chen, C.; Fan, T.; Yan, X.; Lu, H. Research on motion inhibition method using an innovative type of mooring system for spar floating offshore wind turbine. *Ocean Eng.* **2021**, *223*, 108644. [CrossRef]
8. Yang, H.S.; Alkhabbaz, A.; Edirisinghe, D.S.; Tongphong, W.; Lee, Y.H. FOWT Stability Study According to Number of Columns Considering Amount of Materials Used. *Energies* **2022**, *15*, 1653. [CrossRef]
9. Muliawan, M.J.; Karimirad, M.; Moan, T.; Gao, Z. STC (Spar-Torus Combination): A combined spar-type floating wind turbine and large point absorber floating wave energy converter—Promising and challenging. In Proceedings of the International Conference on Offshore Mechanics and Arctic Engineering, Rio de Janeiro, Brazil, 1–6 July 2012; American Society of Mechanical Engineers: New York, NY, USA, 2012; Volume 44946, pp. 667–676.
10. Luan, C.; Michailides, C.; Gao, Z.; Moan, T. Modeling and analysis of a 5 MW semi-submersible wind turbine combined with three flap-type wave energy converters. In Proceedings of the International Conference on Offshore Mechanics and Arctic Engineering, San Francisco, CA, USA, 8–13 June 2014; American Society of Mechanical Engineers: New York, NY, USA, 2014; Volume 45547, p. V09BT09A028.
11. Gao, Z.; Moan, T.; Wan, L.; Michailides, C. Comparative numerical and experimental study of two combined wind and wave energy concepts. *J. Ocean Eng. Sci.* **2016**, *1*, 36–51. [CrossRef]
12. Wan, L.; Gao, Z.; Moan, T.; Lugni, C. Comparative experimental study of the survivability of a combined wind and wave energy converter in two testing facilities. *Ocean Eng.* **2016**, *111*, 82–94. [CrossRef]
13. Li, J.; Shi, W.; Zhang, L.; Michailides, C.; Li, X. Wind–wave coupling effect on the dynamic response of a combined wind–wave energy converter. *J. Mar. Sci. Eng.* **2021**, *9*, 1101. [CrossRef]
14. Chen, M.; Wang, R.; Xiao, P.; Zhu, L.; Li, F.; Sun, L. Numerical analysis of a floating semi-submersible wind turbine integrated with a point absorber wave energy convertor. In Proceedings of the ISOPE International Ocean and Polar Engineering Conference, ISOPE, Virtual, 11–16 October 2020.

15. Hallak, T.S.; Gaspar, J.F.; Kamarlouei, M.; Calvário, M.; Mendes, M.J.; Thiebaut, F.; Guedes Soares, C. Numerical and experimental analysis of a hybrid wind-wave offshore floating platform's hull. In Proceedings of the International Conference on Offshore Mechanics and Arctic Engineering, Madrid, Spain, 17–22 June 2018; American Society of Mechanical Engineers: New York, NY, USA, 2018; Volume 51326, p. V11AT12A047.
16. Gaspar, J.F.; Kamarlouei, M.; Thiebaut, F.; Soares, C.G. Compensation of a hybrid platform dynamics using wave energy converters in different sea state conditions. *Renew. Energy* **2021**, *177*, 871–883. [CrossRef]
17. Kamarlouei, M.; Gaspar, J.F.; Calvario, M.; Hallak, T.S.; Mendes, M.J.; Thiebaut, F.; Soares, C.G. Experimental study of wave energy converter arrays adapted to a semi-submersible wind platform. *Renew. Energy* **2022**, *188*, 145–163. [CrossRef]
18. Zhang, H.; Zhang, N.; Cao, X. Conceptualization and dynamic response of an integrated system with a semi-submersible floating wind turbine and two types of wave energy converters. *Ocean Eng.* **2023**, *269*, 113517. [CrossRef]
19. Ghafari, H.R.; Ghassemi, H.; Abbasi, A.; Vakilabadi, K.A.; Yazdi, H.; He, G. Novel concept of hybrid wavestar-floating offshore wind turbine system with rectilinear arrays of WECs. *Ocean Eng.* **2022**, *262*, 112253. [CrossRef]
20. Ghafari, H.R.; Ghassemi, H.; He, G. Numerical study of the Wavestar wave energy converter with multi-point-absorber around DeepCwind semisubmersible floating platform. *Ocean Eng.* **2021**, *232*, 109177. [CrossRef]
21. Yang, Y.; Bashir, M.; Michailides, C.; Li, C.; Wang, J. Development and application of an aero-hydro-servo-elastic coupling framework for analysis of floating offshore wind turbines. *Renew. Energy* **2020**, *161*, 606–625. [CrossRef]
22. Luan, C. Design and Analysis for a Steel Braceless Semi-Submersible Hull for Supporting a 5-MW Horizontal Axis Wind Turbine. Ph.D. Thesis, Norwegian University of Science and Technology, Trondheim, Norway, 2018.
23. Li, D.; Patton, R. Model Predictive Energy-Maximising Tracking Control for a Wavestar-Prototype Wave Energy Converter. *J. Mar. Sci. Eng.* **2023**, *11*, 1289. [CrossRef]
24. ANSYS AQWA. *AQWA Theory Manual 15317*; AQWA: Canonsburg, PA, USA, 2023.
25. Faltinsen, O. *Sea Loads on Ships and Offshore Structures*; Cambridge University Press: Cambridge, UK, 1993.
26. Li, Y.C.; Teng, B. *The Effect of Waves on Marine Buildings*, 3rd ed.; Ocean Publication: Beijing, China, 2015; pp. 270–273.
27. Wang, Y.; Zhang, L.; Michailides, C.; Wan, L.; Shi, W. Hydrodynamic Response of a Combined Wind–Wave Marine Energy Structure. *J. Mar. Sci. Eng.* **2020**, *8*, 253. [CrossRef]
28. Morison, J.R.; Johnson, J.W.; Schaaf, S.A. The force exerted by surface waves on piles. *Pet. Trans. Aime* **1950**, *2*, 149–154. [CrossRef]
29. Gao, W.; Dong, L.; Huang, J. *ANSYS AQWA Software Introduction and Improvement*; China Water Resources and Hydropower Press: Beijing, China, 2018.
30. Liu, T.; Halse, K.H.; Leira, B.J.; Jiang, Z. Comparative study of the mating process for a spar-type floating wind turbine using two alternative installation vessels. *Appl. Ocean Res.* **2023**, *132*, 103452. [CrossRef]
31. Moriarty, P.J.; Hansen, A.C. *AeroDyn Theory Manual*; National Renewable Energy Laboratory (NREL): Golden, CO, USA, 2005.
32. Yan, X.; Chen, C.; Yin, G.; Ong, M.C.; Ma, Y.; Fan, T. Numerical investigations on nonlinear effects of catenary mooring systems for a 10-MW FOWT in shallow water. *Ocean Eng.* **2023**, *276*, 114207. [CrossRef]
33. Mazarakos, T.P.; Tsaousis, T.D.; Mavrakos, S.A.; Chatjigeorgiou, I.K. Analytical investigation of tension loads acting on a TLP floating wind turbine. *J. Mar. Sci. Eng.* **2022**, *10*, 318. [CrossRef]
34. Liu, H.; Chen, M.; Han, Z.; Zhou, H.; Li, L. Feasibility study of a novel open ocean aquaculture ship integrating with a wind turbine and an internal turret mooring system. *J. Mar. Sci. Eng.* **2022**, *10*, 1729. [CrossRef]
35. Robertson, A.; Jonkman, J.; Masciola, M.; Song, H.; Goupee, A.; Coulling, A.; Luan, C. *Definition of the Semi-Submersible Floating System for Phase II of OC4*; National Renewable Energy Lab. (NREL): Golden, CO, USA, 2014.
36. Kim, H.C.; Kim, M.H. Comparison of simulated platform dynamics in steady/dynamic winds and irregular waves for OC4 semi-submersible 5 MW wind-turbine against DeepCwind model-test results. *Ocean Syst. Eng.* **2016**, *6*, 1–21. [CrossRef]
37. ABS. *Guide for Building and Classing Floating Offshore Wind Turbines*; The American Bureau of Shipping: Houston, TX, USA, 2020.
38. DNVGL-RP-C205. *Environmental Conditions and Environmental Loads*; DNV GL: Høvik, Norway, 2017.